



Contents lists available at ScienceDirect

International Journal of Forecasting

journal homepage: www.elsevier.com/locate/ijforecast

A data-driven approach to forecasting ground-level ozone concentration

Dario Marvin, Lorenzo Nespoli, Davide Strepparava, Vasco Medici*

Scuola Universitaria Professionale della Svizzera Italiana, Switzerland

ARTICLE INFO

Keywords:

Shapley values
Genetic algorithms
Environmental forecasting
Evaluating forecasts
Multivariate time series

ABSTRACT

The ability to forecast the concentration of air pollutants in an urban region is crucial for decision-makers wishing to reduce the impact of pollution on public health through active measures (e.g. temporary traffic closures). In this study, we present a machine learning approach applied to forecasts of the day-ahead maximum value of ozone concentration for several geographical locations in southern Switzerland. Due to the low density of measurement stations and to the complex orography of the use-case terrain, we adopted feature selection methods instead of explicitly restricting relevant features to a neighborhood of the prediction sites, as common in spatio-temporal forecasting methods. We then used Shapley values to assess the explainability of the learned models in terms of feature importance and feature interactions in relation to ozone predictions. Our analysis suggests that the trained models effectively learned explanatory cross-dependencies among atmospheric variables. Finally, we show how weighting observations helps to increase the accuracy of the forecasts for specific ranges of ozone's daily peak values.

© 2021 The Author(s). Published by Elsevier B.V. on behalf of International Institute of Forecasters. This is an open access article under the CC BY license (<http://creativecommons.org/licenses/by/4.0/>).

1. Introduction and motivations

Ground-level ozone (O_3), which forms in the troposphere by photochemical reactions in the presence of sunlight and precursor pollutants, such as the oxides of nitrogen (NO_x) and volatile organic compounds (VOCs) (Calvert, Orlando, Stockwell, & Wallington, 2015), is known to be a pollutant particularly dangerous to human health (Stewart et al., 2017; World Health Organization, 2003). Forecasting ozone concentrations is an important task to ensure the protection of outdoor workers who are exposed to polluted air during the most dangerous hours of the day, as well as sensitive people such as children or the elderly.

In this paper, we tested a number of machine learning algorithms that forecast the maximum hourly ozone

concentration of a given day by performing the prediction at two different times: the evening before and the early morning of the target day. We are particularly interested in the days in which the ozone concentration is significantly higher than usual, due to their potential impact on public health. The choice of the target variable is based on Swiss legislation, which states that the 1-hour mean of $120 \mu\text{g}/\text{m}^3$ must not be exceeded more than once per year (The Swiss Federal Council, 1985). We use an empirical, data-centric approach that leverages a large dataset of air quality, weather station measurements, and weather forecasts. Data are collected for seven sites in southern Switzerland, for which the forecast is performed.

We use Shapley values and a genetic algorithm to select the most important features for each model, and we calculate various forecasts with the help of cutting-edge forecasting algorithms.

The work is organized as follows: Section 1.1 contains an overview of similar research in the scientific literature, and Section 1.2 highlights the contributions we

* Corresponding author.

E-mail address: vasco.medici@supsi.ch (V. Medici).

bring to this work. Section 2 introduces the dataset and the nomenclature we use in the paper to refer to the different features, and Section 3 presents the forecasting problem peculiarities and the problem formulation. Section 4 describes the two feature selection methods that were tested, namely a custom genetic algorithm and a feature selection method based on Shapley values. Section 5 outlines the regression algorithms used to perform the analysis. Section 6 introduces the deterministic and probabilistic key performance indicators (KPIs) that we used to evaluate the different forecasters. Section 7.1 presents the results of the two tested feature selection algorithms. In Section 7.2 we study how different features and feature interactions affect the final predictions of the forecast, using Shapley values. In Section 7.3, we show the numerical results for the tested forecasting algorithms, while in Section 7.4 we focus on predictions of extreme events. Finally, Section 8 concludes the paper with a summary of our main findings.

1.1. Related works

Tropospheric ozone concentration has been the subject of several studies, both for prediction (the task of finding a map from a set of covariates to a target) and for forecasting (predicting the values of the target in advance, in future time steps). In Al Abri, Edirisinghe, Nawadha, and Kingdom (2015) different non-parametric models from the WEKA toolkit were tested to derive the ozone concentration from a set of eight different gaseous chemicals and atmospheric conditions measured at a single location. Similarly, WEKA was used in Mohan and Saranya (2019) to adapt models representing atmospheric conditions to the ozone concentration at ground level, which showed that even summer ozone peaks can be accurately predicted if the atmospheric conditions are known. In Feng, Zhang, Sun, and Zhang (2011), meteorological data from a site near Beijing were used to predict the hourly ozone concentration at that point by using a neural network whose weights were trained using a genetic algorithm. In addition, different models were adapted for different times of the day. In Sheta, Faris, Rodan, Kovač-Andrić, and Al-Zoubi (2018), a nonlinear state-space model using PM₁₀, temperature, wind speed, and relative humidity as inputs was identified by using a neural network to predict ozone concentration. The model was then compared with linear models and a multilayer perceptron. In Siwek and Osowski (2016) the authors used a dataset of 55 characteristics (meteorological conditions and their statistical transformations) collected in Warsaw to predict various air pollutants. They showed that by reducing the number of features with a pre-selection step, the final accuracy of the prediction could be increased. Two pre-selection methods were compared: a genetic algorithm and a stepwise greedy strategy for linear models.

The task of forecasting PM_{2.5} and ozone concentrations for three large Chinese cities was considered in Lv, Cobourn, and Bai (2016). Like in our study, the authors considered multiple monitoring stations, but the final values of the relevant atmospheric variables were weighted averages of neighbors of the target cities. The forecasts

were obtained by fitting knowledge-based empirical formulae using historical data. No systematic investigation of the interaction of variables was carried out. The authors showed how the maximum daily temperature is the single most relevant variable in predicting (and forecasting) ozone concentration. They consistently found a strong correlation between the numerical weather prediction forecast error of this value and the error for ozone prediction. In Eslami, Choi, Lops, and Sayeed (2019) the authors proposed a deep convolutional neural network (CNN) to forecast the hourly ozone concentrations for the day ahead, over 25 monitoring sites. Despite the ability of the CNN to predict daily ozone trends correctly, the authors found that it under-predicted high ozone peaks during the summer. In Gong and Ordieres-Meré (2016), the authors focused on forecasts of extreme ozone concentrations, which are also the most useful to predict. Forecasting extreme events is, in fact, more complicated than predicting them, as demonstrated in Mohan and Saranya (2019). When one is mostly interested in predicting these tail events, sampling techniques can be applied in order to mitigate the class imbalance problem (rare events are under-represented in the training data). The authors of this study applied different sampling methods to increase the classification accuracy of ozone concentration, considering three different classes. They found that under-sampling can indeed increase the classification performance. Unfortunately, a drawback of this technique is that several data of the most represented class are discarded, which could lead to a lack of generalization of the model, due to over-fitting or a reduction of cross-learning (learning patterns from data in a given class, which are also present in a second unobserved class, which could increase the prediction accuracy).

1.2. Contributions

In the presence of a high number of relevant features, the task of forecasting the next-day peak in the concentration of ozone becomes highly challenging, due to the low number of observations on which a forecasting algorithm can be trained. In fact, having a dataset consisting of a few years of observations could result in having a number of features higher than the number of observations, as in the presented case. On the other hand, observations further back in time may not be representative of the current situation, as the mixture of nitrogen oxides in the air has changed over time following vehicle fleet renewal. As a consequence, due to the scarce number of instances, we could not apply under-sampling techniques, as done in Mohan and Saranya (2019). The only effective way to train a model is by applying dimensionality reduction techniques. Our first contribution consists of evaluating two different methods to perform feature selection. First, we tested a genetic algorithm, as was done in Siwek and Osowski (2016) for the pollutant prediction task. In this case, we crafted custom mutation and crossover functions tailored to the forecasting task. The second approach we tested is based on Shapley values (Lundberg & Lee, 2017). We then evaluated and compared the two feature selection methods. To show that the feature selection step is beneficial in increasing the accuracy of

Table 1
Geographic context of air quality and weather monitoring stations.

Station	Code	Altitude [m a.s.l.]	Context	Main O ₃ source
Locarno	l_1	200	Urban	Industry
Brione	l_2	486	Suburb	Valley floor
Bioggio	l_3	314	Suburb	Industry
Tesserete	l_4	518	Rural	Valley floor
Chiasso	l_5	230	Urban	Industry
Mendrisio	l_6	354	Suburb	Industry
Sagno	l_7	704	Rural	Valley floor

the predictive algorithm, we compared our models with two control cases: one in which the model uses all the available features and one in which we pick the features entirely at random. Our second contribution is to compare the performance of different popular learning algorithms trained on the selected features. Third, we investigate the effect of imposing weights on the observations with the highest daily ozone concentration on the algorithms' forecasting quality of extreme values. Our final contribution is an a posteriori explanation of feature importance. We investigate the more relevant feature interactions in predicting the ozone peak and explain our findings in terms of atmospheric physics.

2. Dataset

2.1. Geographical context and data acquisition

In this study, we focused on the Canton of Ticino, the southernmost canton of Switzerland. In this region, the concentration of air pollutants is generally higher than in the rest of the country and is influenced by both the orography and the level of urbanization and industrialization. The natural shield provided by the Alps makes Ticino the region with the highest solar radiation rate in Switzerland. Ticino is characterized by a densely populated and heavily trafficked southern region, and by a sparsely populated and more mountainous northern region. It borders Lombardy to the south, the most industrialized region in Italy.

In this study, we used data acquired from several air quality and weather stations distributed in the region. In addition, the Swiss Federal Office of Meteorology and Climatology MeteoSwiss¹ numerical weather prediction (NWP) service provided weather forecasts for some of these locations. Fig. 1 shows the position of the monitoring stations and the locations for which the weather forecasts are available. Tables 1 and 2 describe the geographical context for the monitoring stations and the weather forecasting locations, respectively.

Due to its photochemical origin, O₃ shows a strong seasonal pattern, with higher concentrations in summer. For this reason we focused our analysis only on the period from May to September in the years between 2015 and 2019. This period was chosen to take into account a significant number of measurements, i.e. enough to train the

Table 2
Geographic context of weather forecasting locations.

Location	Code	Altitude [m a.s.l.]	Context
Comprovasco	p_1	575	Rural
Matro	p_2	2171	Mountain
Bioggio	p_3	518	Suburb
Tesserete	p_4	626	Rural
Chiasso	p_5	240	Urban
Sagno	p_6	704	Suburb

Table 3
Dataset description. The symbol † denotes a variable that is both measured and forecasted by the NWP service, while the symbol ‡ indicates a signal that is only forecasted.

Signal	Symbol	Unit
Nitrogen oxide	NO	[$\mu\text{g}/\text{m}^3$]
Nitrogen dioxide	NO ₂	[$\mu\text{g}/\text{m}^3$]
Generic nitrogen oxides	NO _x	[ppb]
Ozone	O ₃	[$\mu\text{g}/\text{m}^3$]
† Global irradiance	G	[W/m ²]
† Atmospheric pressure	P	[hPa]
† Precipitation	Prec	[mm]
† Relative humidity	RH	[%]
† Temperature	T	[°C]
‡ Dew point	TD	[°C]
† Wind direction, vectorial average	Wd	[°]
† Wind speed, vectorial average	Ws	[m/s]
† Cloud cover	CN	[–]

algorithms correctly, while simultaneously avoiding the use of previous years, when the emissions of precursors NO, NO₂, and NO_x in Switzerland were more intense than today. We used data from the first four years to train the forecasting algorithms and data from 2019 to test them.

A variety of signals covering weather and air quality with hourly resolution were considered for the model, as shown in Table 3. Most monitoring stations record the full set of signals specified in Table 3 on site. The few exceptions, where some signals were not collected locally, were managed with data from the nearest available stations. When training forecasting algorithms, we considered data measured up to 72 h in the past (except for the ARIMAX model) and weather forecasts up to 33 h in the future. The value of 72 h was chosen based on preliminary results, in which we considered a history length up to seven days, and systematically shortened it. As we did not experience significant improvements in accuracy from using a history length higher than 72 h, we fixed this value for all the experiments. Table 3 shows the available signals.

For various reasons, such as station maintenance, data transmission failure, or power outages, some of the data in the time series of the years from 2015 to 2019 are missing. During the training period, data completeness is above 99%, but two stations have substantial data holes in 2019: in Tesserete and Sagno, respectively, 50 and 15 full days of measurements are missing during the test period. All the missing data in the training set were filled using a random forest with surrogate splits, trained to predict the missing data using the station itself and its neighbors.

2.2. Feature engineering

The large number of signals and their high granularity resulted in a high dimensionality of the dataset. To reduce

¹ <https://www.meteoswiss.admin.ch/>.

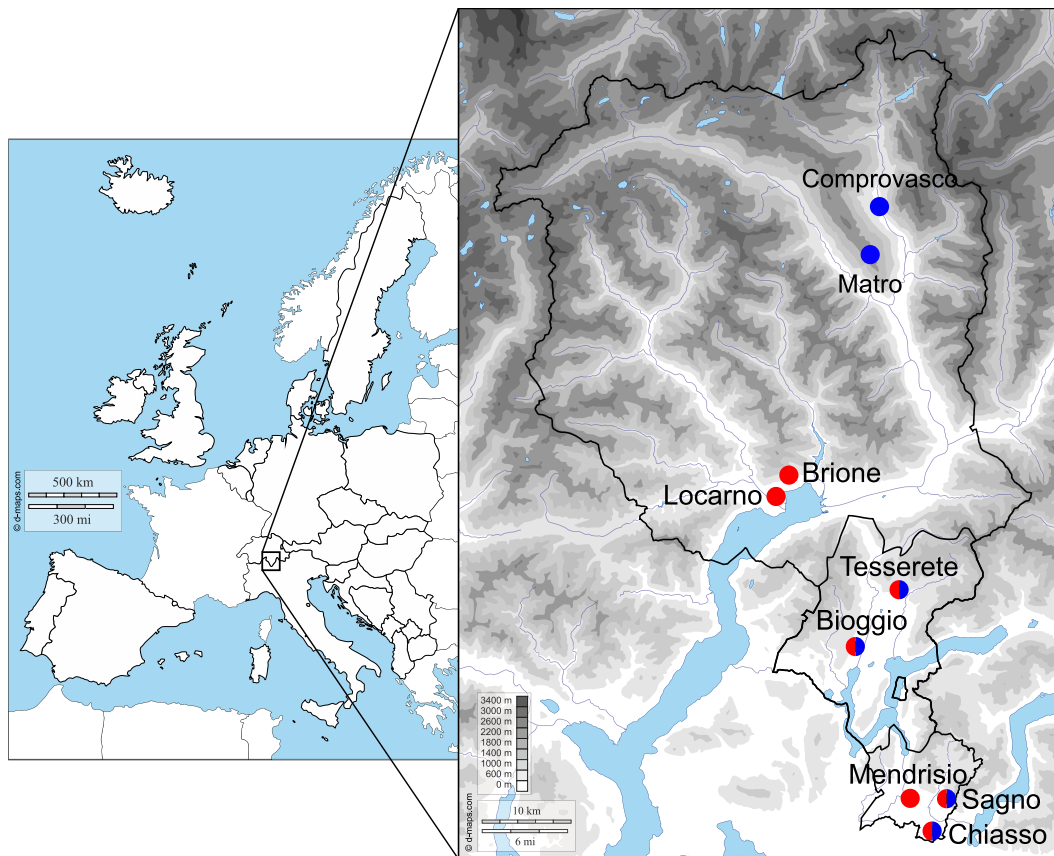


Fig. 1. Map of Ticino with the locations of stations used in the study. Red shows the stations where air quality and weather measurements are collected, and blue shows the locations for which weather forecasts are available. The maps were originally downloaded from *d-maps-1* (2020a) and *d-maps-2* (2020b). (For interpretation of the references to colour in this figure legend, the reader is referred to the web version of this article.)

the overall number of features and minimize the computational effort, we partly replaced the hourly values of the measured and forecasted signals with basic statistical aggregations, i.e. minimum, maximum, and average values over a longer time period, as illustrated in Table 4.

Based on suggestions from experts in the field of atmospheric physics,² we further manipulated some of the signals available in the dataset to create additional features. The engineered features are listed in Table 4. In addition, we included a categorical feature, called *RHW*, which describes the general situation of the weather in Switzerland for the prediction day using 12 weather types.

For each location, separate forecasting models are trained using a subset of the matrix of all features. This subset contains data specific to the location and information from the neighboring stations. For NWP, hourly values are used for the specific location, while bins are used for the data of the neighboring stations, as summarized in Table 4. For example, the dataset of Chiasso contains the hourly NWP from Chiasso itself and bins aggregations from Sarno.

Given the different number of stations involved each time, the number of features for each model is variable and comprise between 1700 and 2100.

2.3. Nomenclature

The ozone forecast at any station for any given day *D* is computed twice: first at 18:30 (16:30 UTC) on the previous day *D* – 1, which we call the *EVE* forecast, and second at 06:30 (04:30 UTC) on the same day *D*, here called the *MOR* forecast. This is because the weather forecasts issued by the NWP services are published twice a day, at 05:00 and at 14:00 local time. Fig. 2 illustrates the time window for a generic day. For each station, we tested eight different prediction methods at both prediction times, *EVE* and *MOR*, for a total of 16 models per station.

When labeling the aggregated data in Table 4, we use the following conventions. Measured quantities are denoted by the letter *m* and weather forecasts provided by NWP services are denoted by the letter *s*. The index is the difference in hours between the last available data point and the acquisition time. Following this convention, *m*₀ refers to the last measured data point available, i.e. the value measured at 06:00 for the *MOR* forecast and at 18:00 for *EVE* forecast. Likewise, *m*₁ refers to the value measured at 05:00 and 17:00, and so on up to *m*₂₃.

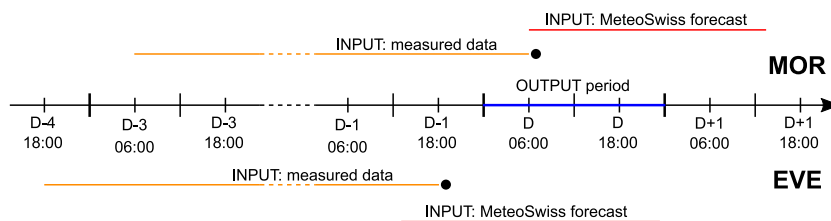
The same temporal indexing applies to values provided by NWP services. For *MOR* we call *s*₀ the forecasted value at 06:00, *s*₁ the value for 07:00, and so on. In the *EVE* case we call *s*₀ the predicted value at 18:00, *s*₁ the predicted

² Environment Observatory of Southern Switzerland (OASI).

Table 4

Summary of all the features used in this study. More information about the MOR and EVE cases is given in Section 2.3.

Signal kind	Time interval	Code	Aggregation
All measured data	Past 24 h (m_0, \dots, m_{23})	m_i	Hourly values
	From 0 to 24 h before	24h	Mean
	From 0 to 48 h before	48h	
	From 0 to 72 h before	72h	
All forecasts (same station)	MOR: from s_0 to s_{32} EVE: from s_0 to s_{29}	s_i	Hourly values
All forecasts (neighboring station)	MOR: from s_0 to s_7 EVE: from s_0 to s_6	b_1	Minimum, maximum and average of every bin b_i
	MOR: from s_8 to s_{16} EVE: from s_7 to s_{13}	b_2	
	MOR: from s_{17} to s_{24} EVE: from s_{14} to s_{19}	b_3	
	MOR: from s_{25} to s_{32} EVE: from s_{20} to s_{29}	b_4	
Measured NOx	MOR: previous afternoon (m_6 to m_{18}) EVE: previous morning (m_6 to m_{18})	NOx_{12h}	Mean
Forecasted T	MOR: upcoming afternoon (s_6 to s_{18}) EVE: upcoming afternoon (s_{18} to s_{29})	$\hat{T}_{PM}, \hat{T}_{PM,squared}$	Mean and squared mean
Forecasted T	MOR: all hourly values, from s_0 to s_{32} EVE: all hourly values, from s_0 to s_{29}	\hat{T}_{max}	Maximum
Forecasted TD	MOR: all hourly values, from s_0 to s_{32} EVE: all hourly values, from s_0 to s_{29}	$\hat{TD}_{max}, \hat{TD}_{max}^{transf}$	Maximum, (Maximum + 20) ³
Forecasted G	MOR: upcoming morning (s_0 to s_6) MOR: upcoming afternoon (s_6 to s_{18}) EVE: upcoming morning (s_6 to s_{18}) EVE: upcoming afternoon (s_{18} to s_{29})	$\hat{G}_{AM}, \hat{G}_{PM}$	Mean
Forecasted CN	MOR: upcoming morning (s_0 to s_6) MOR: upcoming afternoon (s_6 to s_{18}) EVE: upcoming morning (s_6 to s_{18}) EVE: upcoming afternoon (s_{18} to s_{29})	$\hat{CN}_{AM}, \hat{CN}_{PM}$	Mean
Forecasted $Prec$	Upcoming 24 h (s_0 to s_{23})	$\hat{Prec}_{24h,sum}$	Sum
Measured YO3	O ₃ measurements of the previous day	YO3	Maximum
Forecasted RHW	One categorical value for the prediction day	RHW	–

**Fig. 2.** Time window of input and output data. Times are given in local time (CEST).

value at 19:00, and so on. The structure of the aggregation bins is shown in Table 4.

To better refer to each specific component of the models, we denote the features based on the location of the measurement and time to which it is referred, combining the codes of Tables 3, 4, 1, and 2. For example, G_{m1}^I designates the global irradiance measured in Locarno at 05:00 in the MOR model and at 17:00 in the EVE model. Similarly, \hat{T}_{s10}^{p3} is the forecasted temperature in Bioggio at 16:00 in the MOR model, and at 04:00 on the following day in the EVE model. NO_{72h}^2 is the mean value of all

the measured NO concentrations up to 72 h before the prediction, in Brione.

3. Problem formulation

The problem of forecasting the daily maximum ozone signal presents the following characteristics:

1. The signal is strongly seasonal, due to the presence of annual patterns in both anthropogenic and non-anthropogenic processes governing ozone generation.

2. The signal is non-stationary, since its variance is subject to inter- and intra-annual fluctuations.
3. The forecasts' dependence on the features is non-linear, as described in the literature and as further detailed in Section 7.2.
4. The forecasted values are physically bounded by the photo-chemistry and advective phenomena regulating the formation and transport of ozone in the troposphere and atmosphere.
5. In our use case, monitoring stations providing measurements of relevant features for ozone forecasting, such as temperature, past ozone and NOx values, are not sufficiently dense (nor at similar distances from prediction points) to provide a regular mesh, as can be seen in Fig. 1. In this case, the use of spatio-temporal Gaussian processes (Kupilik & Witmer, 2018), Gaussian Markov random fields (Cameletti, Lindgren, Simpson, & Rue, 2013), or other graph-based spatio-temporal techniques (Carrillo et al., 2020) can lead to poor results.

Given the above considerations, we chose to model daily ozone maxima using separate predictors for each location, while still taking into account relevant features from nearby locations. The neighboring stations for each prediction point are illustrated in Fig. 1, where the whole region is divided into three macro-zones. In any case, we let the feature selection processes described in Section 4 discriminate whether a given measurement station is relevant. Calling n the number of observations and k the number of features, we define a training and a test dataset, $\mathcal{D}_{tr} = \{x_{tr}, y_{tr}\}$ and $\mathcal{D}_{te} = \{x_{te}, y_{te}\}$, respectively, where $x_{tr} \in \mathbb{R}^{n_{tr} \times k}$ and $x_{te} \in \mathbb{R}^{n_{te} \times k}$ are matrices of features, and $y_{tr} \in \mathbb{R}^{n_{tr}}$ and $y_{te} \in \mathbb{R}^{n_{te}}$ are the target vectors, containing the maximum hourly ozone concentration of the same days. In this paper, n_{tr} and n_{te} are equal to 587 and 151, respectively, that is, the number of available days between May and September for the 2015–2018 period and for 2019. On the other hand, the number of features, k , is fixed at 30 for all the numerical experiments and raised to 100 for the study of predicting high peaks, described in Section 7.4. These numbers were chosen experimentally by systematically increasing them and choosing the k value beyond which the predictors' performance no longer increased significantly.

We train a model $f(x_{tr}, \Theta)$, where Θ is a set of the model's parameters, in order to produce the forecasts for unseen data $x_{te} \in \mathbb{R}^{n_{te} \times k}$:

$$\hat{y}_{te} = f(x_{te}, \Theta). \quad (1)$$

In order to compare the results across the different approaches, we used regression-specific key performance indicators (KPIs), as classification scores can only be compared while using the same bins for the choice of the classes. Different values for the bins' edges are used in the ozone prediction literature, since those are typically chosen based on the local legislation. As such, we trained the model $f(x_{tr}, \Theta)$ minimizing L2 loss:

$$\Theta^* = \underset{\Theta}{\operatorname{argmin}} \|y_{tr} - f(x_{tr}, \Theta)\|_2^2. \quad (2)$$

We highlight how this notation must be slightly adapted for the ARIMAX model introduced in Section 5; in this

case the model can be described as $f(x_{tr}, y_{tr}, \Theta)$, where the endogenous input signal y_{tr} is then opportunely shifted with the use of the backshift operator, as further explained in Section 5.

4. Feature selection methods

Given the large number of features in each model, if we were to train the prediction algorithms using all the variables, whose number largely exceeds the number of available observations, we could potentially incur numerical problems of solution non-uniqueness and multicollinearity that would corrupt the prediction process. Moreover, even if the dataset contained a proportional number of observations, an excessive number of features would still result in a long computational time, which is justified only if the forecasting performance is better than that of an algorithm trained on a subset of the features.

We decided to perform feature selection using a custom implementation of a genetic algorithm (GA), as well as using a proceeding issued from game theory, exploiting Shapley values. The effectiveness of these two approaches is compared in Section 7.1 against a model composed of features picked at random and a model composed of all the available features.

4.1. Feature selection using a genetic algorithm

In our implementation of the GA, an individual A is defined as a subset of the entire feature set F with cardinality k :

$$A \subset F, \quad |A| = k \quad (3)$$

where k is the number of retained features. As anticipated in Section 3, in this study we set $k = 30$.

We defined a crossover function that ensures that the offsprings that emerge from it still retain k features from their parents, with no repetitions. Formally, the offspring C is a subset of the union of the sets of its parents A and B , with cardinality k :

$$C \subset (A \cup B), \quad |C| = k \quad (4)$$

We defined a custom mutation function so that each feature of the offspring C is either the original feature of its parent A with probability 95%, or a new feature from $B \subset (F \setminus A)$ with probability 5%, and such that C has only unique features. In practice, we generate two sequences a and b from the sets A and B , by randomly fixing their order, and iterate on them to generate the new set C , which is composed of the elements of the sequence c , where the i th element of c is defined as:

$$c_i = a_i(u \geq 0.05) + b_i(u < 0.05) \quad u \sim U[0, 1] \quad (5)$$

The fitness function is defined as the out-of-bag mean squared error (MSE) of a random forest composed of 30 bootstrap-aggregated (bagged) decision trees, trained on the k active features of the individuals. We selected a population size of 10k individuals, a crossover fraction of 80%, and an elite count of 5% of the population size. The GA stops after 100 stall generations and the feature set of the best individual is selected.

4.2. Feature selection using Shapley values

Another method to assess the importance of each feature is presented in [Lundberg and Lee \(2017\)](#). This method assigns feature importance scores using Shapley values, which originated in the field of game theory where they are used to estimate the contribution of various agents in increasing the welfare of a community. These are expressed as:

$$\phi_i(f, x_{tr}) = \sum_{z \subseteq x} \frac{|z|! (k - |z| - 1)!}{k!} [f(z, \theta) - f(z \setminus i, \theta)] \quad (6)$$

where $f(x_{tr}, \theta)$ is a regression model, in our specific case the NGBoost algorithm, which is introduced in Section 5; x_{tr} is the feature set on which the model has been trained; θ is a model-specific set of parameters; k is the number of variables in the training set x_{tr} ; and $z \setminus i$ denotes the minus set operation, that is, the subtraction of the i th feature from the reduced dataset z . The authors in [Lundberg and Lee \(2017\)](#) showed that such coefficients have highly desirable properties that favorably affect their ability in the (local) explanation of the models, and have been shown to be consistent and more robust with respect to other more widespread methods for the evaluation of feature importance. Furthermore, the authors in [Lundberg et al. \(2020\)](#) recently proposed a computationally efficient algorithm specifically tailored for tree-based models, and made it available through the shap Python package. The shap package provides an exact computation of Shapley value explanations for tree-based models. This provides local explanations with theoretical guarantees of local accuracy and consistency, which increase the robustness of the method, since it does not rely on random samplings, which would be required to find the Shapley values using approximate algorithms.

5. Regression models

After the k features that best explain the data are selected, we use them to create the regression matrix and produce the test forecasts. For this work, we studied the output of several parametric models, such as linear regression, ridge regression, LASSO, and ARIMAX, as well as more complex non-parametric tree-based algorithms, such as random forests, XGBoost, NGBoost, and LSBoost, as described below.

Penalized linear regression algorithms. Ridge regression is a method designed to avoid collinearity issues and avoid near-singular matrix inversions when solving linear regression problems, especially in the case in which the number of features is large compared to the number of observations. In this case, the regression coefficients $\beta \in \mathbb{R}^k$ are quadratically penalized with parameter λ , such that the closed-form solution becomes:

$$\hat{\beta}_R = (x_{tr}^T x_{tr} + \lambda I_k)^{-1} x_{tr}^T y_{tr}, \quad (7)$$

where I_k is an identity matrix of size k . In this work, λ is tuned in cross-validation on the training set. Instead of punishing β using the L2 norm, least absolute

shrinkage and selection operator (LASSO) regression ([Tibshirani, 1996](#)) penalizes β using the L1 norm, such that some of the elements of $\hat{\beta}$ can be set to zero. Unlike ridge regression, LASSO does not have a closed-form solution, but rather must be approximated through numerical methods.

ARIMAX. The well-known autoregressive integrated moving average with explanatory variable (ARIMAX) is defined as:

$$\hat{y}_t = \beta x_{tr} + \sum_{i=1}^p \phi_i B^i(y'_t) - \sum_{i=1}^q \theta_i \epsilon_{t-1} + \epsilon_t. \quad (8)$$

where B is the backshift operator, i.e. $B^n(z_t) = z_{t-n}$; ϵ_t is additive white Gaussian noise; and the time series y' is the result of differencing y_{tr} d times. The matrix x_{tr} contains the daily values of the selected features up to the day before the prediction, and β denotes the regression coefficients as usual.

The models are created and calculated with statsmodels's SARIMAX function, and the parameters p , q , and d are chosen via grid search and fitted using maximum likelihood estimation; we considered only $d = 0$, since we do not have important trends, while we set 7 and 3 as maximum values for p and q , respectively. We stress that, even if the features contained in x_{tr} refer to the last 72 h, the ARIMAX model has been left free to extend the endogenous signal's influence on the forecast up to seven previous days, that is $p = 7$. However, for all the considered locations, the grid search returned $p \leq 3$.

Random forests and quantile random forests. The random forest (RF) algorithm independently fits several decision trees, each trained on different datasets, created from the original one through random re-sampling of the observations, and keeping only a fraction of the overall features, chosen at random ([Hastie, Tibshirani, & Friedman, 2009](#)). The final prediction of the RF is then a (possibly weighted) average of the trees' responses. One important variant of RF algorithms is quantile regression forests (QRF). The main difference from RF is that QRF keeps the value of all the observations in the fitted trees' nodes, not just their mean, and assesses the conditional distribution based on this information. Here, we used the Matlab TreeBagger class, which implements the QRF algorithm described in [Meinshausen \(2014\)](#).

Tree-based boosting algorithms. Boosting algorithms employ additive training: starting from a constant model, at each iteration, a new tree or any other so-called "weak learner" $h_k(x)$ is added to the overall model $F_k(x)$, so that $F_{k+1}(x) = F_k(x) + \eta h_k(x)$, where $\eta \leq 1$ is a hyperparameter denoting the learning rate, which helps reduce over-fitting. The least-squares gradient boosting (LSBoost) algorithm applies boosting in functional space: each weak learner h tries to learn the gradient (with respect to the previous model $F_k(x)$) of the least-squares loss function. In other words, h_k is fitted on the overall prediction error at iteration $k - 1$.

A different approach is used by the XGBoost algorithm ([Chen & Guestrin, 2016](#)), which fits the additive

model $F_k(x)$ in parameter space, that is, using a second-order approximation of the loss, as a function of the parameters of the weak learners (decision trees). This approximation and other techniques used by XGBoost (like an approximate histogram search for selecting splitting points in the trees) result in a speedup of the training process, with respect to LSBoost or RF algorithms, without sacrificing accuracy. At the same time, the algorithm introduces quadratic penalization on the parameter's value and on the overall complexity of the trees, with which parameters can be tuned to further mitigate over-fitting.

In addition to the QRF algorithm, we used a second algorithm that is able to assess the conditional probability distribution of the predictions: natural gradient boosting (NGBoost) (Duan et al., 2019). While none of the previous algorithms introduced assumptions on the probability distribution of the observations, NGBoost explicitly fits the parameters of a parametric probability distribution on each observation. This is made possible by exploiting the tree structure of the underlying weak learner, since observations in the same leaves share the same probability distribution parameters. The algorithm is fitted in functional space, but instead of directly learning the maximum likelihood gradient, the authors propose to correct it with the Fisher information. This results in fitting the so-called natural gradient, which makes the learning process invariant to reparametrization of the underlying probability distribution.

We fitted LSBoost models using Matlab's `fitrensemble` function, tuning its hyper-parameters via Bayesian optimization and using five-fold cross-validation. The XGBoost and NGBoost algorithms were fitted using their official `xgboost` and `ngboost` Python packages, respectively, and hyper-parameters were selected using a grid search, always using a five-fold cross-validation strategy. We highlight that tuning the hyper-parameters in cross-validation mitigates over-fitting issues with the regression algorithms.

6. Key performance indicators

The performance of the forecasting algorithms introduced in Section 5 was evaluated using the following standard performance indicators:

$$\text{RMSE} = \sqrt{\frac{1}{n} \sum_{i=1}^n (\hat{y}_i - y_i)^2} \quad (9)$$

$$\text{MAE} = \frac{1}{n} \sum_{i=1}^n |\hat{y}_i - y_i| \quad (10)$$

$$\text{MAPE} = \frac{100\%}{n} \sum_{i=1}^n \left| \frac{y_i - \hat{y}_i}{y_i} \right| \quad (11)$$

$$S = 1 - \frac{\text{RMSE}}{\text{RMSE}_{\text{pers}}} \quad (12)$$

$$A = \frac{100\%}{n} \sum_{i=1}^n \mathbb{1} \{C(\hat{y}_i) = C(y_i)\} \quad (13)$$

where RMSE is the root mean squared error, MAE is the mean absolute error, MAPE is the mean absolute

percentage error, S denotes forecast skill, and A denotes accuracy. $\text{RMSE}_{\text{pers}}$ is the RMSE of the persistence model, i.e. the model where the prediction at day $D + 1$ is equal to the measured value at day D . $C(y_i)$ is the function that associates every measured or forecasted value to the respective class, explicitly given by

$$C(y_i) = \begin{cases} 1 & \text{if } 0 < y_i \leq 60, \\ 2 & \text{if } 60 < y_i \leq 120, \\ 3 & \text{if } 120 < y_i \leq 135, \\ 4 & \text{if } 135 < y_i \leq 180, \\ 5 & \text{if } 180 < y_i \leq 240, \\ 6 & \text{if } 240 < y_i. \end{cases} \quad (14)$$

These values are the thresholds of classes of increasing severity of air pollution, as indicated by the Swiss Society of Air Protection Officers (CercI'Air) (Swiss Society of Air Protection Officers, 2019). Class 3 is especially narrow compared to the other classes. As a result it will be harder for the regression forecasting algorithms to correctly predict this class.

Finally, we evaluated those algorithms which also returned conditional distributions—that is, QRF and NGBoost—using two additional KPIs. The first KPI is the reliability (Pinson, McSharry, & Madsen, 2010), defined as

$$R(\tau) = \frac{1}{n} \sum_{i=1}^n \mathbb{1} \{y_i < \hat{y}_{i,\tau}\}, \quad (15)$$

where $\hat{y}_{i,\tau}$ is the quantile predicted by the algorithm at the level $\tau \in [0, 1]$. This KPI calculates how many of the total number of measured values are indeed lower than the quantile predicted on the same observations. If the forecasting algorithm were perfect, the $R(\tau)$ curve would lie on the bisector of the first quadrant.

The second probabilistic KPI is the average quantile loss function, also known as pinball loss (Bentzen & Friederichs, 2014):

$$\bar{\rho}(\tau) = \frac{1}{n} \sum_{i=1}^n \rho_\tau(y_i - \hat{y}_{i,\tau}), \quad (16)$$

where the function $\rho_\tau(x)$ is defined as

$$\rho_\tau(x) = \begin{cases} \tau |x| & \text{if } x \geq 0, \\ (1 - \tau) |x| & \text{if } x < 0, \end{cases} \quad (17)$$

This KPI measures how narrow the predicted probability density function is around the observations. It can be shown that this loss is minimized, independently of the underlying distribution which generated the data, when the predicted quantiles are the true ones. It should be noted that for $\tau = 0.5$, the corresponding value $\bar{\rho}(\tau)$ is half the value of the MAE statistic. To further evaluate the performance of the quantiles as a single score, we integrate $\bar{\rho}(\tau)$ over the $[0, 1]$ interval, as outlined in Gneiting and Raftery (2007). Thus we define

$$\text{Q-score} = \int_0^1 \bar{\rho}(\tau) d\tau. \quad (18)$$

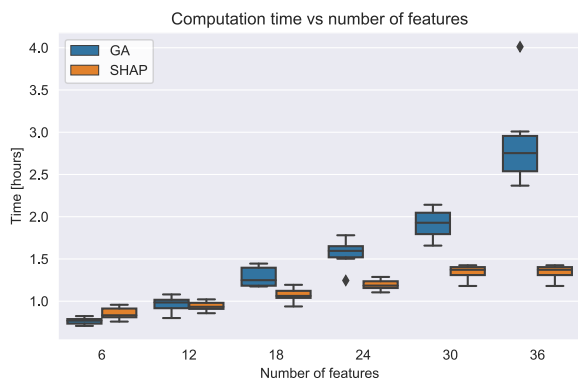


Fig. 3. Boxplots for the computational time as a function of an increasing number of features k and feature selection method. Each boxplot contains values from seven-fold CV, for three different locations.

7. Results

7.1. Feature number and feature selection methods comparison

To investigate the impact of model complexity on the general quality of the results, we varied the number of features k from 6 to 36 in increments of six. Due to the relatively high computational time required to run this experiment, the models were calculated for only three stations (Bioggio, Chiasso, and Locarno) on data from 2015 to 2018, using seven-fold cross-validation. Fig. 3 shows the computational time, for all the models, as a function of the number of features and the feature selection method, for the three selected stations.

The time needed to perform feature selection and predict the results increases exponentially as a function of the number of features for feature selection based on the GA, while it shows a linear trend for feature selection based on Shapley values. CV computation could take up to 4 h on our machine, a 16-core Intel i9-7960X CPU @ 2.80 GHz with 128 GB of RAM.

Similarly, using features selected with SHAP, we compared the performance of a subset of forecasting algorithms by gradually increasing the number of features (Fig. 4). The errors of the models do not appear to decrease after about 24 features. Consequently, we decided to construct our models for the main analysis with $k = 30$ features. This number is a good compromise between the quality of the model and the computation time.

To investigate whether feature selection effectively improves the quality of prediction and to determine which is the most efficient technique, we compared the performance of the algorithms across all locations using four methods: GA, Shapley values (SHAP), random features, and all available features (no feature selection). For the first three methods, 30 features are either selected according to the corresponding method or picked at random, while in the last case all the available features are used to build the model.

To compare the performance of the different models, we used Nemenyi statistical tests (Hollander & Wolfe,

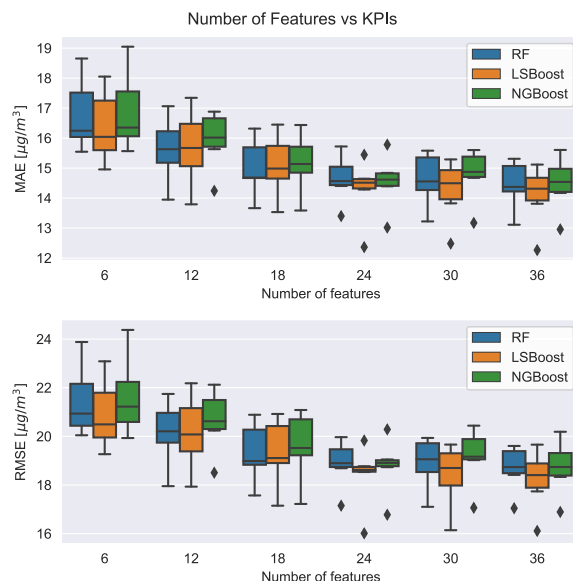


Fig. 4. Boxplots for the MAE and RMSE, with respect to the number of features k . Each boxplot contains values from seven-fold CV, for three different locations.

1999), a post-hoc pairwise test used to compare a set of m different models on a group of n independent experiments. First, a matrix $R \in \mathbb{R}^{n \times m}$ is obtained whose elements $r_{i,j}$ are the ranks for experiment i and model j . Then, the mean rank for each model is retrieved through column-wise averages of R . The performance of the two models is identified as significantly different by the Nemenyi test if the corresponding average ranks differ by at least the critical difference

$$CD = q_{\alpha, m} \sqrt{\frac{m(m+1)}{12n}} \quad (19)$$

where q_{α} is the quantile α of the Studentized range statistic with m samples, here set to $\alpha = 0.9$. We implemented the Nemenyi test in Python following the implementation in the `tsutils` R package (Kourentzes, Svetunkov, & Schaer, 2020). The Nemenyi test is usually performed after Friedman's test, which is a non-parametric analog of variance for a randomized block design; this can be considered a non-parametric version of one-way ANOVA with repeated measures. More details on the difference and implementation of the two tests can be found in Dale (2006).

The results of the Nemenyi test can be observed in Fig. 5. In Table 5, we show the KPIs calculated for a few selected forecasting algorithms for the locations with best, average, and worst RMSE statistics, namely Bioggio MOR, Chiasso MOR, and Mendrisio EVE.

The results show that the approach using Shapley values obtains the best rank for all the ensemble methods across all the locations. For Ridge and LM, we essentially have a tie between SHAP and GA. In the case of LASSO, the approach that uses all features obtains the best rank. This is likely explained by the fact that LASSO, by design, inherently performs feature selection. We can conclude that

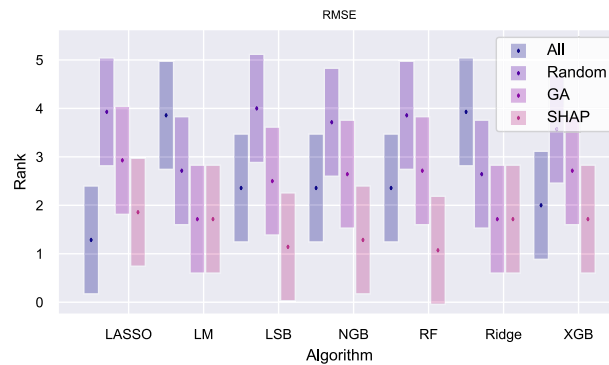


Fig. 5. Nemenyi test for comparing the RMSE performance of the four feature selection methods across all locations.

Table 5

Comparison between different feature selections for the best, average, and worst stations.

		BIO MOR				CHI MOR				MEN EVE			
		SHAP	GA	All	Rand	SHAP	GA	All	Rand	SHAP	GA	All	Rand
LSBoost	MAE	13.46	14.17	14.41	15.58	14.50	15.18	15.27	19.02	16.69	17.24	16.90	19.84
	RMSE	17.68	18.38	18.98	20.35	19.36	21.25	20.03	24.21	21.59	22.61	21.70	24.92
	MAPE	10.34	11.06	11.29	12.32	10.65	11.05	11.33	14.42	12.75	13.57	13.52	15.59
	S	0.430	0.408	0.388	0.344	0.419	0.362	0.399	0.273	0.333	0.302	0.330	0.231
	Accuracy	71.43	68.71	71.43	69.39	71.43	71.43	70.75	60.54	65.07	60.96	59.59	59.59
XGBoost	MAE	14.05	14.32	14.63	15.55	15.84	15.66	17.34	21.13	16.78	17.69	17.54	21.43
	RMSE	18.58	19.01	19.44	21.09	20.87	21.26	21.58	26.27	22.23	22.80	22.27	26.94
	MAPE	10.91	11.17	11.67	12.24	11.77	11.54	12.95	16.56	13.05	13.66	14.01	16.88
	S	0.401	0.387	0.373	0.320	0.374	0.362	0.352	0.212	0.314	0.296	0.313	0.169
	Accuracy	68.71	72.79	65.99	70.07	70.07	70.07	69.39	57.14	65.75	62.33	60.27	56.85
NGBoost	MAE	13.85	14.38	15.02	15.64	15.04	15.88	15.85	18.72	16.12	17.05	17.54	20.14
	RMSE	18.50	18.70	20.04	20.60	19.90	21.64	21.11	23.58	21.32	22.79	22.76	25.46
	MAPE	10.73	11.13	11.96	12.36	11.06	11.85	11.98	14.26	12.54	13.29	14.12	16.04
	S	0.404	0.397	0.354	0.336	0.403	0.351	0.367	0.292	0.342	0.297	0.298	0.214
	Accuracy	68.71	68.71	68.71	68.03	69.39	70.07	67.35	59.86	66.44	60.27	58.90	57.53

performing a preliminary feature selection using Shapley values analysis is preferable in terms of KPI quality and computation time. The SHAP feature selection is faster compared to GA and All and avoids needlessly slowing down the predictive algorithms.

7.2. Feature importance and interactions

To assess the importance of each feature in predicting the maximum ozone concentration, we again applied the shap library introduced in Section 4.2, using the NGBoost algorithm as the $f(x_{tr}, \theta)$ regression model. We thus analyzed the most relevant features for the seven locations and their interactions. Table 6 summarizes the three most relevant features for the considered locations. For five of the considered cases, the most important feature was a value of forecasted temperature for both the MOR and EVE predictions. For the other cases, the most important feature was a past value of ozone concentration. The three most relevant features include forecasted values of the temperature, locally or at a nearby station, and past measured ozone concentrations for all the locations.

7.2.1. Temperature influence

In Fig. 6, we show the influence of single observations on the ozone forecast, divided by feature, for the location of Chiasso. The most relevant predictor is $\hat{T}_{b_2, mean}^{p_6}$,

Table 6

Three most relevant features for the MOR and EVE predictions for the seven considered locations. Colors refer to the two dominant classes of variables. Green: NWP forecasted temperature, blue: measured ozone.

Location		f1	f2	f3
BIO	MOR	$\hat{T}_{b_2, mean}^{p_4}$	$NO2_{m_0}^{l_3}$	$\hat{T}_{s_{14}}^{p_4}$
	EVE	$\hat{T}_{s_{25}}^{p_4}$	$\hat{T}_{b_4, mean}^{p_4}$	$O3_{m_0}^{l_3}$
CHI	MOR	$\hat{T}_{b_2, mean}^{p_6}$	$O3_{m_{11}}^{l_5}$	$\hat{T}_{s_{12}}^{p_5}$
	EVE	$\hat{T}_{b_4, mean}^{p_6}$	$O3_{m_1}^{l_5}$	$\hat{T}_{s_{23}}^{p_5}$
MEN	MOR	$\hat{T}_{b_2, mean}^{p_6}$	$\hat{T}_{s_{12}}^{p_6}$	$NO2_{m_0}^{l_5}$
	EVE	$\hat{T}_{b_4, mean}^{p_6}$	$O3_{m_1}^{l_5}$	\hat{G}_{PM}^p
LOC	MOR	$\hat{T}_{b_2, mean}^{p_2}$	$\hat{T}_{b_1, mean}^{p_2}$	$\hat{T}_{s_{10}}^{p_2}$
	EVE	$\hat{T}_{b_4, max}^{p_2}$	$O3_{m_0}^{l_1}$	$\hat{T}_{s_{19}}^{p_1}$
BRI	MOR	$\hat{T}_{s_8}^{p_2}$	$\hat{T}_{b_2, mean}^{p_2}$	$\hat{T}_{s_7}^{p_1}$
	EVE	$\hat{T}_{b_4, max}^{p_2}$	$\hat{T}_{s_{19}}^{p_1}$	$\hat{T}_{s_{21}}^{p_1}$
SAG	MOR	$\hat{T}_{b_4, max}^{p_2}$	$O3_{m_{13}}^{l_7}$	$YO3^{l_7}$
	EVE	$O3_{m_1}^{l_7}$	$O3_{m_0}^{l_7}$	$O3_{24h}^{l_7}$
TES	MOR	$O3_{24h, mean}^{l_4}$	$\hat{T}_{s_{15}}^{p_4}$	$Wd_{s_3}^{p_4}$
	EVE	$O3_{m_0}^{l_4}$	$\hat{T}_{s_{25}}^{p_4}$	$\hat{T}_{s_{26}}^{p_4}$

which is the forecasted temperature at a nearby location.

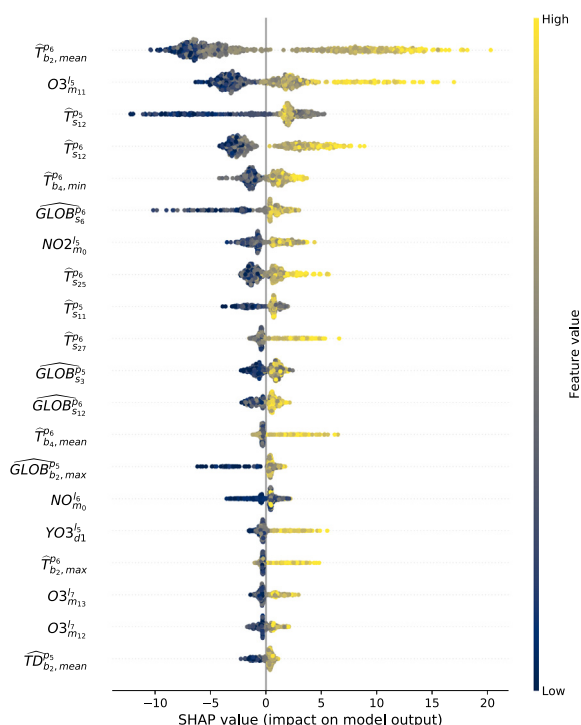


Fig. 6. Feature importance for each observation, for Chiasso MOR.

Several chemical reactions and pathways influence the chemistry of ozone formation and removal in the troposphere (Crutzen, Lawrence, & Pöschl, 1998; Lu, Zhang, & Shen, 2019; Monks et al., 2015), such that imputing temperature's influence to just one of them is hardly satisfactory; other factors and processes must be considered. Photochemical processes are dominant factors in determining the ozone peak concentrations, together with thermal and radiative conditions. Other more physical processes, such as local wind systems and diurnal boundary layer dynamics, are of secondary importance in our study, since it focuses on the generally well-mixed diurnal boundary layer. We aim to forecast the peak concentrations under well-mixed afternoon conditions, rather than variations in ozone concentration within the diurnal cycle. We stress that some phenomena, like the role of the effective height of the boundary layer for the air mass characteristics (precursor mixture, photochemical reactivity), determining the volume available to dilute the emissions, and the role of large-scale advection, are not directly considered by the forecasting algorithms, and that our analysis is limited to the variables selected by the feature selection procedure. However, since the temperature is causally correlated with the height of the boundary layer, we indirectly account for some of its effect by using temperature as a predictor. Fig. 7 shows the Shapley values for the mean value of the temperatures forecasted in Sagno between 14:00 and 23:00, and the interaction with the mean forecasted temperature in Chiasso at 17:00. We can observe how the influence of the forecasted temperature on the maximum O_3 peak does not follow the

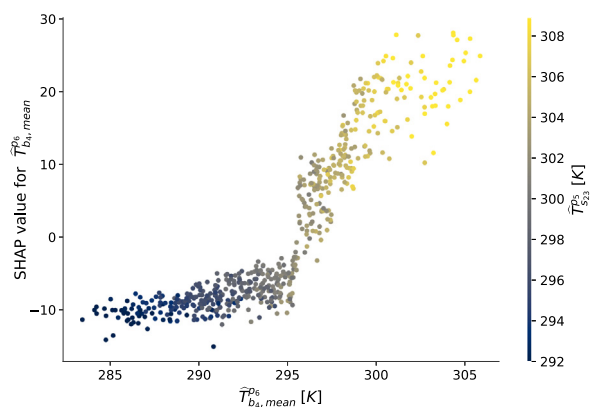


Fig. 7. Feature importance interaction between the mean of forecasted temperatures in Sagno between 14:00 and 23:00, and forecasted temperature in Chiasso at 17:00, on the EVE prediction of ozone in Chiasso.

typical exponential form of a chemical rate constant, but rather a sigmoid. A similar sigmoid-like functional relation between these two variables can be observed in all the other locations. This functional form can be explained by explicitly modeling the main chemical reactions involved in the formation and destruction of O_3 , and their temperature-dependent rate coefficients. The authors in Pusede et al. (2014), Pusede, Steiner, and Cohen (2015) modeled the interdependence of the O_3 production rate, NO_x , and temperature. Initially, they modeled the main chemical tropospheric O_3 formation processes. Then, they replaced the volatile organic compounds (VOC) reactivity with a functional relation learned from observations between the latter and daily maximum temperature. They found a sigmoid-like influence between the daily maximum temperature on O_3 production, for concentrations of NO_x greater than 6 ppb. A similar sigmoid-like dependence of O_3 formation rates and the temperature was found in Walcek and Yuan (1995), both considering or disregarding a linear correlation between the maximum daily temperature and solar irradiance (Fig. 4a and Fig. 5 in the reference, respectively). In all these studies, the authors kept the influence of other variables (e.g. VOC concentration and irradiance) fixed, or treated them as parameters. This is equivalent to performing a sensitivity analysis on the rate of change of O_3 , which is exactly the scope of the Shapley variables. In this sense, the findings of the aforementioned authors are compatible with Fig. 7. We stress that the sigmoid-like importance of temperature in predicting O_3 concentrations cannot be directly extracted from the raw data. To better explain this, we show in Fig. 8 a partial dependence plot of the measured O_3 , that is, the target variable and the measured temperature. As we can see, the raw data show an exponential-like relation, very similar to what was found in Walcek and Yuan (1995), Fig. 1a, where measurements of maximum hourly O_3 concentrations and temperatures from the New Jersey urban region are plotted.

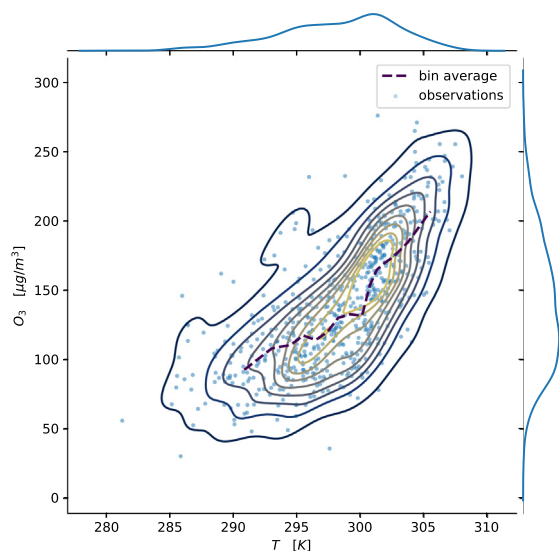


Fig. 8. Partial dependence plot between instantaneously measured T and O_3 in Chiasso. Continuous lines are iso-density surfaces estimated with a kernel density estimator.

7.2.2. NO_2 importance interactions

Solar irradiance and NO_x concentration play a major role in the photochemistry of tropospheric ozone (Crutzen et al., 1998; Walcek & Yuan, 1995). In Figs. 9 and 10, the influence of the measured NO_2 and its interaction with forecasted temperature on the MOR prediction of O_3 in Bioggio and Sagno is shown. We can see for both cases how the sigmoid-like NO_2 importance becomes more pronounced for increasing forecasted temperatures. This means that at high concentrations of NO_2 , higher temperatures accelerate the O_3 formation rate. On the other hand, Figs. 9 and 10 suggest that at low concentrations of NO_2 , O_3 generation from NO_2 becomes increasingly important with increasing temperature, with respect to other O_3 formation concurring processes. As such, low NO_2 concentrations are more significant predictors of low O_3 concentrations at high ambient temperatures. These conclusions cannot be explained with the same kind of analysis as that carried out in Pusede et al. (2015) for example, where only the O_3 formation rate with respect to NO_x and temperature was investigated, rather than its relative importance over other concurrent photochemical pathways.

7.3. Performance of the regression models

In Table 7 we present the results of our study with respect to the KPIs introduced in Section 6, obtained by first applying the SHAP feature selection approach described in 4.2.

In general, the two algorithms that perform the best overall are LSBoost and NGBoost, since most of the lowest MAE and RMSE values and the highest accuracy values are concentrated in these two algorithms. In the station of Tesserete, nearly one-third of the total ozone measurements in the summer of 2019 were unavailable, so the

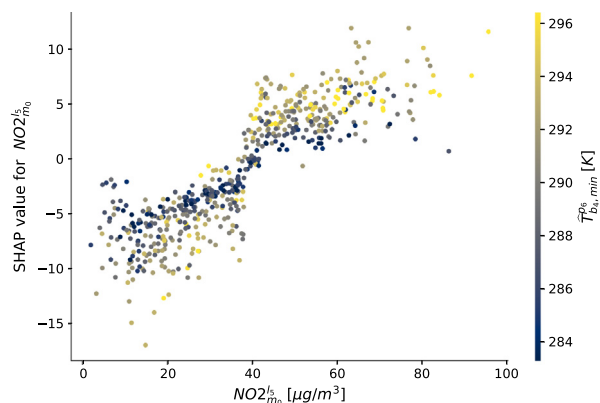


Fig. 9. Feature importance interaction between measured NO_2 in Chiasso and temperature forecasted in Sagno, on the MOR prediction of ozone in Mendrisio.

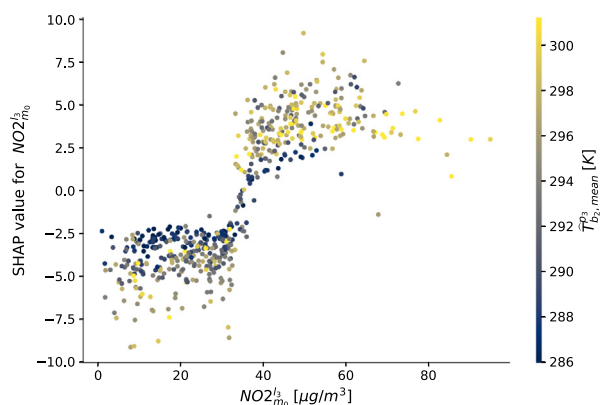


Fig. 10. Feature importance interaction between measured NO_2 in Bioggio and temperature forecasted in Sagno, on the MOR prediction of ozone in Bioggio.

results are not directly comparable with those of the other stations.

Table 7 shows that, for the same algorithm, the MOR results are generally better than the EVE counterpart, although the difference in some cases is slight. This is not surprising, since the MOR predictions also use the data gathered overnight, which are not available to the EVE forecasters. However, there is an exception in Brione, where the MAE statistic is slightly higher at MOR for all the ensemble algorithms. The best results are obtained in Bioggio, where both MOR and EVE forecasts have the best KPIs across all the stations.

The relatively small differences between MOR and EVE seem to indicate that the data gathered during the night are not particularly important. In fact, as Table 6 shows, the three most important features for each model essentially revolve around ozone measured during the peak of the previous day and forecasted temperature. In all models, much importance is given to the forecasts of the upcoming afternoon and the measured ozone values of the previous afternoon. Arguably, the NWP forecasts are more precise in the morning, thus leading to more precise ozone predictions as well.

Table 7

Main results of the study with Shapley values feature selection. Values in boldface indicate the lowest RMSE for the corresponding location.

		BIO		CHI		MEN		LOC		BRI		SAG		TES	
		MOR	EVE	MOR	EVE	MOR	EVE	MOR	EVE	MOR	EVE	MOR	EVE	MOR	EVE
RF	MAE	13.81	15.28	15.20	15.82	15.70	16.10	14.08	14.43	14.52	14.71	14.88	15.37	13.64	15.03
	RMSE	18.07	19.82	20.21	21.66	20.54	21.30	18.33	19.01	19.03	20.20	19.48	20.62	19.41	21.63
	MAPE	10.74	11.83	11.13	11.69	12.35	12.65	11.78	12.36	12.49	12.80	11.93	12.25	12.08	13.82
	S	0.418	0.364	0.394	0.352	0.364	0.342	0.394	0.374	0.404	0.370	0.295	0.256	0.201	0.114
	Accuracy	69.39	67.81	66.67	65.75	65.99	62.33	68.03	62.33	66.67	67.12	61.76	62.22	66.33	65.98
	Q-score	4.987	5.396	5.452	5.765	5.590	5.749	5.133	5.239	5.208	5.364	5.259	5.662	4.494	4.961
LSBoost	MAE	13.46	13.96	14.50	15.56	14.66	16.69	14.20	14.30	14.25	14.50	15.08	14.59	13.37	14.86
	RMSE	17.68	18.18	19.36	21.03	19.50	21.59	18.58	19.03	18.78	20.53	19.39	19.73	18.89	20.73
	MAPE	10.34	10.78	10.65	11.47	11.54	12.75	11.71	11.98	12.03	12.53	12.09	11.53	11.71	13.44
	S	0.430	0.416	0.419	0.371	0.396	0.333	0.386	0.373	0.412	0.360	0.298	0.288	0.222	0.151
	Accuracy	71.43	67.81	71.43	67.12	66.67	65.07	67.35	69.18	68.03	69.18	61.76	61.48	70.41	64.95
	Q-score	5.947	6.298	6.298	7.485	6.429	7.671	6.453	6.333	6.241	5.979	12.14	12.50	25.94	27.36
XGBoost	MAE	14.05	15.10	15.84	16.80	16.01	16.78	14.81	15.84	15.57	15.18	15.92	16.96	13.73	15.31
	RMSE	18.58	19.58	20.87	22.04	21.45	22.23	18.85	22.21	19.58	21.31	20.25	22.44	19.33	21.27
	MAPE	10.91	11.73	11.77	12.30	12.35	13.05	12.17	13.83	13.17	13.19	12.66	13.73	11.92	13.77
	S	0.401	0.371	0.374	0.341	0.336	0.314	0.377	0.268	0.387	0.335	0.266	0.190	0.204	0.129
	Accuracy	68.71	73.29	70.07	67.12	65.31	65.75	66.67	70.55	68.03	65.07	61.76	56.30	65.31	64.95
	Q-score	5.947	6.298	6.298	7.485	6.429	7.671	6.453	6.333	6.241	5.979	12.14	12.50	25.94	27.36
NGBoost	MAE	13.85	14.83	15.04	16.23	14.84	16.12	14.96	14.02	15.18	15.09	19.57	19.77	19.34	21.76
	RMSE	18.50	19.56	19.90	21.27	19.62	21.32	18.92	18.84	19.78	20.37	25.36	26.44	26.12	28.92
	MAPE	10.73	11.32	11.06	11.94	11.68	12.54	12.42	12.06	12.83	13.08	16.93	16.86	18.37	20.90
	S	0.404	0.372	0.403	0.364	0.393	0.342	0.375	0.379	0.381	0.365	0.082	0.046	−0.07	−0.18
	Accuracy	68.71	69.18	69.39	65.75	65.99	66.44	61.90	67.12	65.31	69.18	47.79	50.37	59.18	52.58
	Q-score	5.947	6.298	6.298	7.485	6.429	7.671	6.453	6.333	6.241	5.979	12.14	12.50	25.94	27.36
LM	MAE	15.27	15.64	17.46	17.49	16.55	26.42	16.12	27.26	15.32	73.43	15.14	14.67	13.01	171.7
	RMSE	21.67	20.32	23.03	23.37	21.74	109.9	20.84	144.2	20.41	693.6	19.78	19.99	19.03	945.3
	MAPE	12.01	12.32	13.38	13.62	12.92	21.12	13.67	22.76	12.95	62.56	12.22	11.60	11.25	154.0
	S	0.301	0.347	0.309	0.301	0.327	−2.39	0.311	−3.75	0.361	−20.6	0.284	0.279	0.217	−37.7
	Accuracy	68.71	65.75	66.67	61.64	65.31	61.64	65.31	65.07	68.71	66.44	63.24	64.44	67.35	17.53
	Q-score	5.947	6.298	6.298	7.485	6.429	7.671	6.453	6.333	6.241	5.979	12.14	12.50	25.94	27.36
LASSO	MAE	15.76	15.91	17.54	17.68	17.94	17.56	15.33	16.26	15.38	18.11	15.59	14.87	12.95	14.18
	RMSE	21.13	20.43	22.99	23.58	23.22	22.89	20.18	21.07	20.73	23.82	20.11	20.32	18.83	20.64
	MAPE	12.30	12.40	13.31	13.45	14.12	14.00	12.99	13.87	13.27	15.79	12.52	11.67	11.35	12.92
	S	0.319	0.344	0.310	0.295	0.281	0.293	0.333	0.306	0.351	0.257	0.272	0.267	0.225	0.155
	Accuracy	65.99	64.38	63.27	61.64	58.50	59.59	65.31	63.70	68.03	62.33	58.82	63.70	65.31	64.95
	Q-score	5.947	6.298	6.298	7.485	6.429	7.671	6.453	6.333	6.241	5.979	12.14	12.50	25.94	27.36
Ridge	MAE	15.23	15.63	17.46	17.47	16.51	26.42	16.12	27.26	15.16	71.56	15.13	14.67	12.97	168.5
	RMSE	21.61	20.32	23.03	23.32	21.70	109.9	20.84	144.2	20.23	670.5	19.77	19.99	19.00	914.6
	MAPE	11.97	12.31	13.38	13.59	12.88	21.12	13.67	22.76	12.83	60.96	12.22	11.61	11.21	151.1
	S	0.304	0.347	0.309	0.302	0.328	−2.39	0.311	−3.75	0.367	−19.9	0.284	0.279	0.218	−36.4
	Accuracy	68.71	66.44	66.67	61.64	65.31	61.64	65.31	65.07	69.39	65.75	64.71	64.44	67.35	16.49
	Q-score	5.947	6.298	6.298	7.485	6.429	7.671	6.453	6.333	6.241	5.979	12.14	12.50	25.94	27.36
ARIMAX	MAE	17.57	16.87	17.12	17.72	16.57	18.05	14.8	14.74	16.3	14.94	16.25	14.38	12.89	13.32
	RMSE	23.34	22.28	23.21	22.77	21.95	23.42	20.39	19.79	22.76	19.73	21.35	19.07	19.17	20.88
	MAPE	13.42	13.05	12.92	13.26	12.44	13.94	12.33	12.43	13.41	12.81	13.09	11.44	10.89	11.6
	S	0.25	0.28	0.3	0.32	0.32	0.28	0.32	0.35	0.29	0.38	0.21	0.29	0.71	0.69
	Accuracy	60.54	63.7	63.95	61.38	63.95	57.24	63.95	68.49	65.31	69.18	56.46	63.7	53.06	58.9
	Q-score	5.947	6.298	6.298	7.485	6.429	7.671	6.453	6.333	6.241	5.979	12.14	12.50	25.94	27.36

Figs. 11, 12, and 13 graphically illustrate the results for the best (Bioggio MOR), average (Chiasso MOR), and worst (Mendrisio EVE) cases. Each figure is composed of four plots. The top one shows a comparison between the main forecasting algorithms and the measured values. The second plot shows the prediction intervals at levels 20%, 40%, 60%, and 80% issued by the RF algorithm as well as the RF prediction. The third and fourth plots further investigate the goodness of fit of the quantiles of the RF and NGBoost algorithms.

7.4. High peaks prediction

The analysis presented so far focused on the dataset in its entirety, aiming to provide the best KPIs over all the data, independently from the air pollution severity class. However, when predicting ozone concentrations, it is generally more important to be able to correctly predict high concentrations, as they can pose a health risk.

For this reason, we decided to prompt the predictor to focus more on high concentrations, in our case classes 4, 5, and 6 as defined in Eq. (14), by introducing weighted training. We assigned different weights to the observations depending on the severity class they were in. We found that it was beneficial to assign a weight $w_1 \in [20, 200]$ to observations in class 6, $w_2 \in [20, 200]$ to observations in class 5, $w_3 \in [10, 20]$ to observations in class 4, and a fixed weight of 1 to all the other observations. The key idea is to find the optimal set of weights w_1, w_2, w_3 for each location and case with improved forecasting quality at high concentrations. The same set of weights is used during feature selection with SHAP and NGBoost and to train the prediction algorithm with the selected features. Applying weights during feature selection should help select the most important features to recognize the highest ozone concentrations.

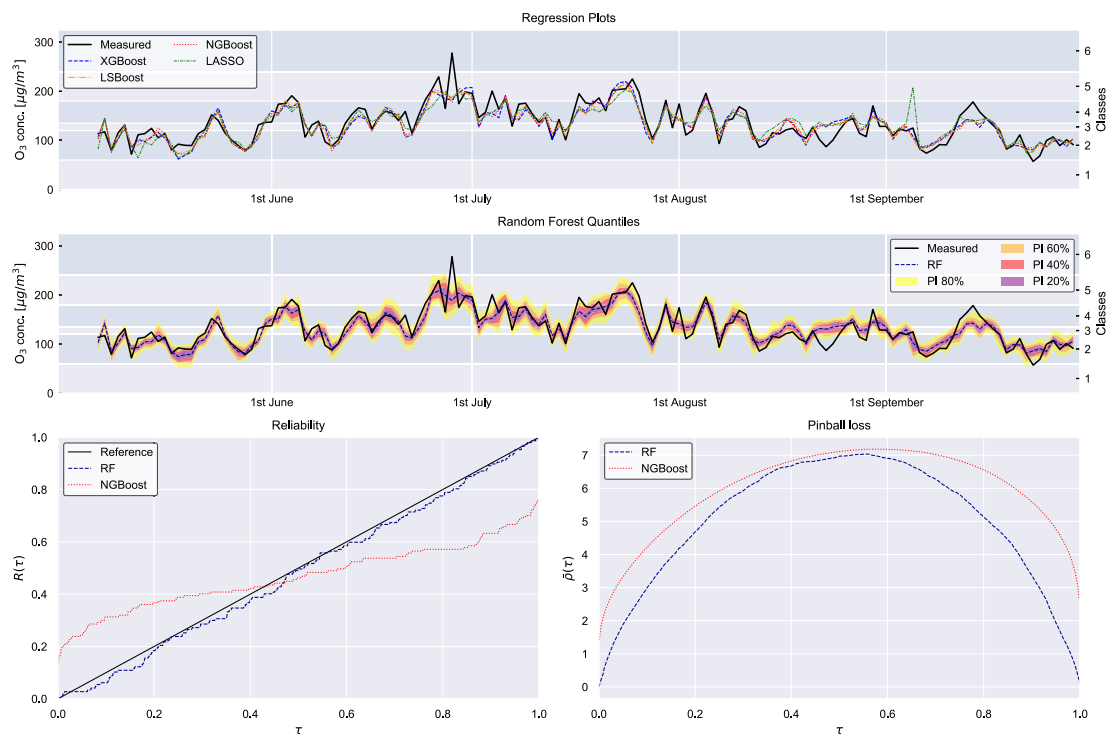


Fig. 11. Result plots of the station yielding the best results, Bioggio MOR.

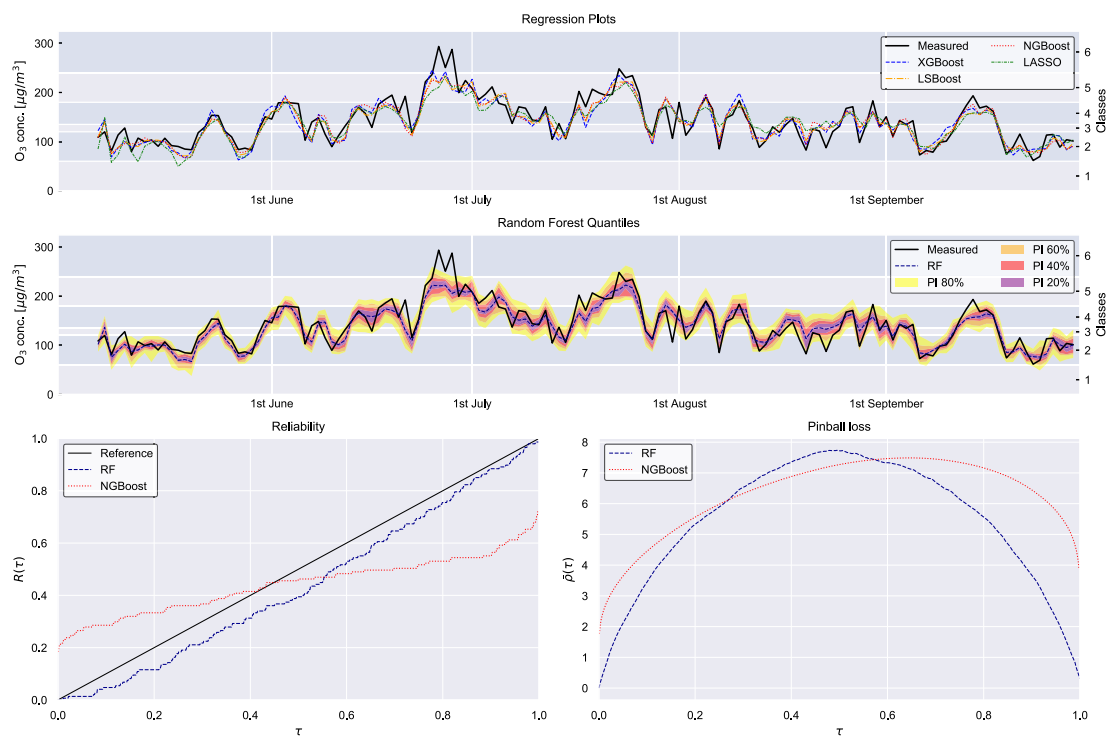


Fig. 12. Result plots of a station yielding average results, Chiasso MOR.

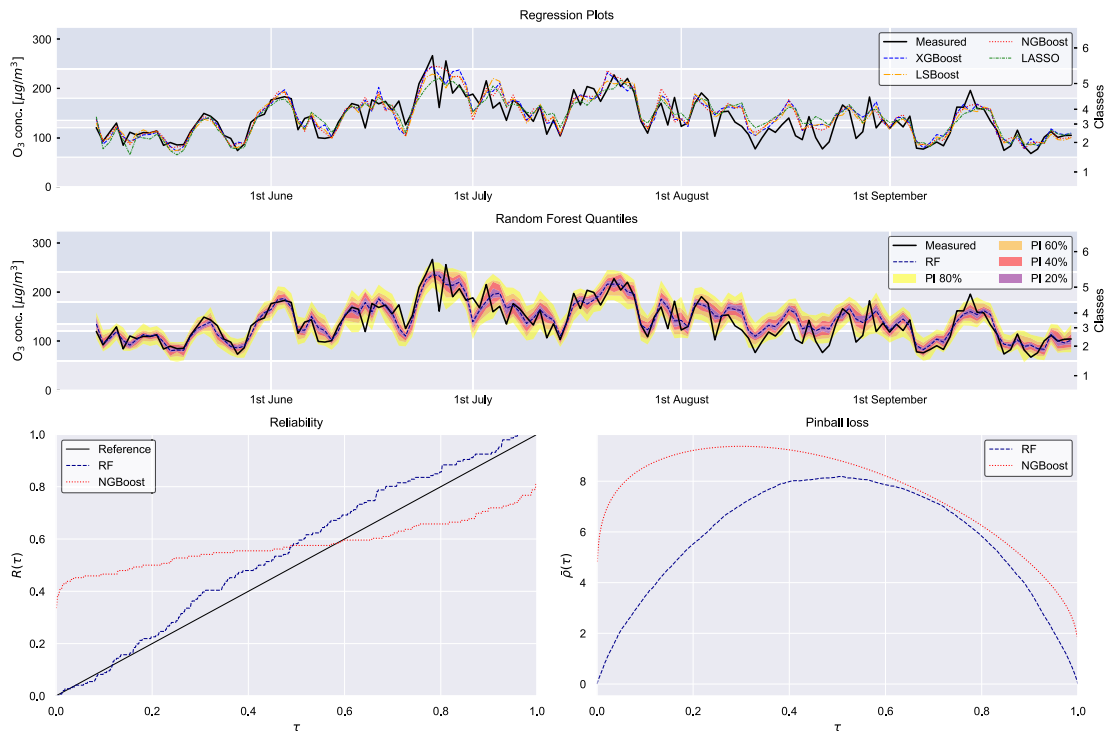


Fig. 13. Result plots of the station yielding the worst results, Mendrisio EVE.

We sought to increase the classification accuracy of three particular subsets of our data using weighted training, by evaluating the best combination of weights to optimize prediction accuracy for the following:

- Values in classes 4, 5, and 6 ($O_3 > 135 \mu\text{g}/\text{m}^3$)
- Values in classes 5 and 6 ($O_3 > 180 \mu\text{g}/\text{m}^3$)
- Values in class 6 ($O_3 > 240 \mu\text{g}/\text{m}^3$)

We analyzed the four stations with the highest number of extreme measurements in 2019: Bioggio, Mendrisio, Locarno, and Chiasso. All these stations registered at least one event of class 6 and many events of class 5, as shown in Table 8. In particular, Chiasso registered 27 measurements above $180 \mu\text{g}/\text{m}^3$, of which four were above $240 \mu\text{g}/\text{m}^3$. In contrast to what we observed with unweighted training, we noticed that when using weighted training, increasing the number of selected features above 30 improved the prediction accuracy at high ozone concentrations. Therefore, we decided to increase to 100 the number of features that the algorithm can use to perform its prediction. We used SHAP as the feature selection method and NGBoost as the regressor. We calculated the KPIs of the models for each combination of the weights w with $w_1, w_2 \in \{20, 40, 60, \dots, 200\}$, $w_3 \in \{10, 20\}$. Fig. 14 shows the aggregated accuracy of the prediction for the three different classes of interest. Figs. 14(a) and 14(b) illustrate the distribution of the accuracy when considering only the ozone measured values above $135 \mu\text{g}/\text{m}^3$. Similarly, Figs. 14(c), 14(d), and 14(e), 14(f) show the accuracy when restricting ourselves only to values above 180 and $240 \mu\text{g}/\text{m}^3$, respectively. The continuous

iso-lines are obtained with cubic interpolation. It is difficult to infer which weights give the best results, especially when trying to maximize the accuracy of observations above $135 \mu\text{g}/\text{m}^3$, but for the other two cases, a high w_2 and variable w_1 give the best weights for observations above $180 \mu\text{g}/\text{m}^3$, whereas a high w_1 and a low w_2 appear to be the best combination of weights for correctly predicting observations above $240 \mu\text{g}/\text{m}^3$.

Table 9 shows the results of weighted training for the considered stations. We report the KPIs and the three sets of weights that gave the best accuracy for each fraction of the dataset, compared to the results obtained in the case where no weights are applied. We can see that the introduction of weights does not unduly affect the KPIs, and in fact improve them in some cases. For Chiasso MOR, we also show in Fig. 15 the complete confusion matrices obtained. It can be seen that when actively trying to enhance the recognition of observations above $135 \mu\text{g}/\text{m}^3$, the correct classification of these values increased from about 50%–75% to about 80%–85%. Similarly, for observations above $180 \mu\text{g}/\text{m}^3$ the correct recognition rate increases from 50%–70% to 80%–90% in all stations but Locarno, where it stops at 70%. Finally, in Mendrisio and Chiasso, we could correctly predict all values above $240 \mu\text{g}/\text{m}^3$, which was not achieved in the unweighted analysis. This is not the case for Bioggio and Locarno, where the only class 6 value is never recognized.

8. Conclusions

In this study, we forecasted the day-ahead maximum ground-level ozone concentration during the summer of

Table 8
Number of particular events registered in the analyzed stations in 2019.

Station	Values above 135 $\mu\text{g}/\text{m}^3$ cl. [4, 5, 6]	Values above 180 $\mu\text{g}/\text{m}^3$ cl. [5, 6]	Values above 240 $\mu\text{g}/\text{m}^3$ cl. 6
Chiasso	46	23	4
Bioggio	47	17	1
Mendrisio	70	22	2
Locarno	41	9	1

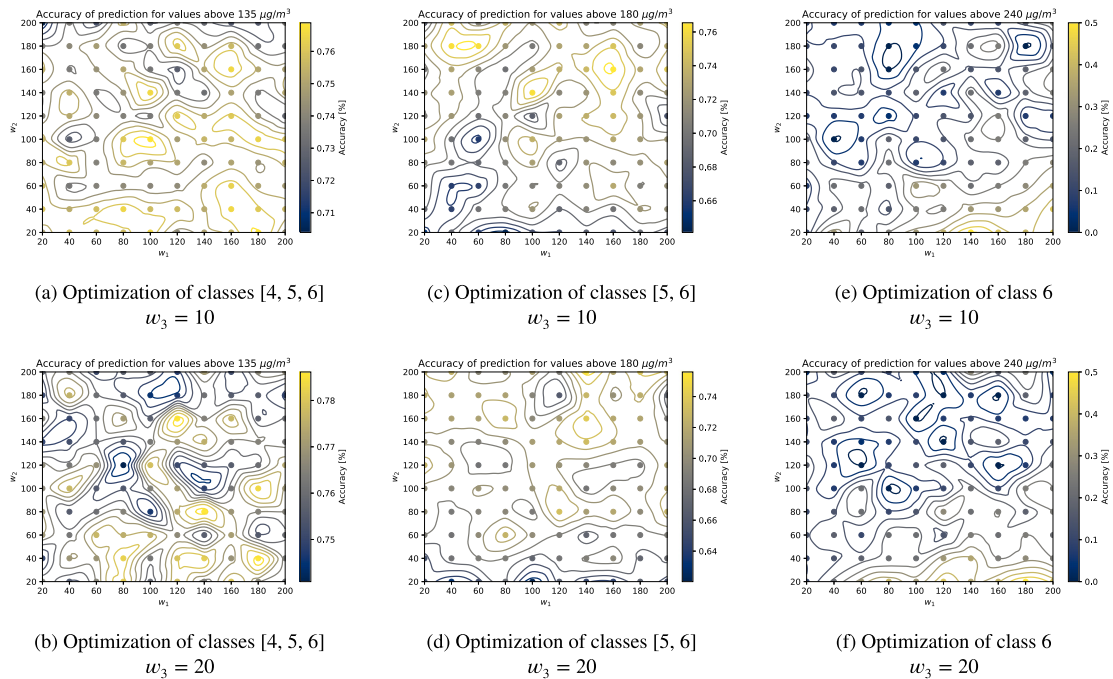


Fig. 14. Plot of the results of the weights grid search with 100 selected features, aggregated across the stations of Chiasso, Bioggio, Mendrisio and Locarno.



Fig. 15. Confidence matrices for Chiasso MOR.

2019 in seven localities in southern Switzerland, using a physics-agnostic, data-driven approach. Due to the high number of signals potentially affecting the predictions, we performed preliminary feature selection using two methods, which we compared. The selected features were then used to train different state-of-the-art forecasting algorithms. Analyzing feature importance interactions using Shapley values suggested that the models trained through our learning pipeline effectively learned explanatory cross-dependencies among atmospheric variables described in the ozone photochemistry literature.

Our analysis showed that gradient boosting algorithms, and in particular least-squares boosting and natural gradient boosting, consistently outperformed the other tested forecasting methods. Where possible, we further compared our results with those of other papers, and we were able to conclude that our results are similar to previous analysis and, in some cases, even better.

We then evaluated the effect of weighted training to increase the accuracy of predictions for high ozone concentrations. Our analysis showed that this method is

Table 9

Results of the weighted analysis.

		Weights			Target class accuracy			KPIs		
		w_1	w_2	w_3	cl. [4, 5, 6]	cl. [5, 6]	cl. 6	MAE	RMSE	Tot. Acc.
BIO MOR	No weights	–	–	–	72.72	61.11	0.00	13.28	17.66	70.95
	Max. accuracy classes [4, 5, 6]	140	80	20	85.07	77.78	0.00	13.03	17.52	73.68
	Max. accuracy classes [5, 6]	120	200	10	79.10	88.89	0.00	13.61	18.25	71.05
	Max. accuracy class 6	180	100	10	77.61	72.22	0.00	12.62	16.18	70.39
BIO EVE	No weights	–	–	–	69.69	61.11	0.00	14.22	18.50	68.71
	Max. accuracy classes [4, 5, 6]	40	100	20	84.84	77.78	0.00	14.59	18.47	73.51
	Max. accuracy classes [5, 6]	60	180	10	83.33	83.33	0.00	15.08	19.27	69.53
	Max. accuracy class 6	80	40	10	83.33	72.22	0.00	14.24	18.31	73.50
CHI MOR	No weights	–	–	–	72.60	55.56	0.00	14.61	18.79	71.52
	Max. accuracy classes [4, 5, 6]	180	20	10	80.82	74.07	75.00	13.75	19.54	75.50
	Max. accuracy classes [5, 6]	140	200	20	79.45	81.48	50.00	15.51	21.33	70.86
	Max. accuracy class 6	200	40	10	75.34	70.37	100.00	13.53	19.14	71.52
CHI EVE	No weights	–	–	–	65.75	48.15	0.00	15.28	20.43	67.35
	Max. accuracy classes [4, 5, 6]	80	20	20	82.19	74.07	75.00	14.90	19.96	71.52
	Max. accuracy classes [5, 6]	200	200	10	75.34	85.19	75.00	15.26	20.13	73.51
	Max. accuracy class 6	180	20	20	75.34	70.37	75.00	15.26	20.09	67.55
MEN MOR	No weights	–	–	–	77.14	68.18	50.00	14.69	19.49	71.62
	Max. accuracy classes [4, 5, 6]	120	40	20	84.29	81.82	100.00	14.17	19.02	71.43
	Max. accuracy classes [5, 6]	180	60	10	80.00	86.36	100.00	14.56	19.40	67.35
	Max. accuracy class 6	200	40	10	77.14	81.82	100.00	14.34	19.23	69.39
MEN EVE	No weights	–	–	–	74.28	72.72	50.00	15.29	19.38	68.02
	Max. accuracy classes [4, 5, 6]	120	120	20	82.86	81.82	50.00	16.13	21.13	67.81
	Max. accuracy classes [5, 6]	200	60	10	74.29	90.91	100.00	16.53	21.06	64.38
	Max. accuracy class 6	180	40	10	81.43	81.82	100.00	15.54	19.75	67.81
LOC MOR	No weights	–	–	–	54.90	40.00	0.00	14.12	18.45	64.86
	Max. accuracy classes [4, 5, 6]	180	100	20	80.39	60.00	0.00	14.43	18.52	72.11
	Max. accuracy classes [5, 6]	40	140	10	72.55	70.00	0.00	15.06	19.65	68.03
	Max. accuracy class 6	60	180	10	70.59	70.00	0.00	13.92	17.97	70.07
LOC EVE	No weights	–	–	–	52.94	40.00	0.00	14.09	18.84	65.99
	Max. accuracy classes [4, 5, 6]	40	80	20	80.39	50.00	0.00	14.37	18.61	69.18
	Max. accuracy classes [5, 6]	60	200	10	76.47	70.00	0.00	14.71	19.83	67.12
	Max. accuracy class 6	100	40	10	66.67	50.00	0.00	13.93	17.75	67.81

feasible, as it increases forecast accuracy without compromising overall forecast quality. Future directions for this work include the formulation of probabilistic techniques for robust estimations of annual ozone concentration peaks, which are the most difficult events to predict, due to their scarcity in the training set. In this view, training forecasters with ad-hoc-generated adversarial examples could result in a better forecast of the conditional probability distributions.

Declaration of competing interest

The authors declare that they have no known competing financial interests or personal relationships that could have appeared to influence the work reported in this paper.

Acknowledgment

This work was funded by the Environment Observatory of Southern Switzerland (OASI, www.ti.ch/oasi) of the Department of Territory of Canton Ticino (DT).

References

- Al Abri, E. S., Edirisinghe, E. A., Nawadha, A., & Kingdom, U. (2015). Modelling ground-level ozone concentration using ensemble learning algorithms. In *International conference on data mining (DMIN)*.

- the steering committee of the world congress in computer science, computer engineering and applied computing (No. x) (pp. 148–154).
- Bentzien, S., & Friederichs, P. (2014). Decomposition and graphical portrayal of the quantile score. *Quarterly Journal of the Royal Meteorological Society*, 140(683), 1924–1934. <http://dx.doi.org/10.1002/qj.2284>.
- Calvert, J. G., Orlando, J. J., Stockwell, W. R., & Wallington, T. J. (2015). *The mechanisms of reactions influencing atmospheric ozone*. Oxford University Press.
- Cameletti, M., Lindgren, F., Simpson, D., & Rue, H. (2013). Spatio-temporal modeling of particulate matter concentration through the SPDE approach. *ASTA. Advances in Statistical Analysis*, 97(2), 109–131. <http://dx.doi.org/10.1007/s10182-012-0196-3>, URL: <http://link.springer.com/10.1007/s10182-012-0196-3>.
- Carrillo, R. E., Leblanc, M., Schubnel, B., Langou, R., Topfel, C., & Alet, P.-J. (2020). High-resolution PV forecasting from imperfect data: A graph-based solution. *Energies*, 13(21), 5763. <http://dx.doi.org/10.3390/en13215763>.
- Chen, T., & Guestrin, C. (2016). XGBoost: A scalable tree boosting system. In *Proceedings of the 22nd ACM SIGKDD international conference on knowledge discovery and data mining* (pp. 785–794). <http://dx.doi.org/10.1145/2939672.2939785>.
- Crutzen, P. J., Lawrence, M. G., & Pöschl, U. (1998). On the background photochemistry of tropospheric ozone. *Tellus, Series B (Chemical and Physical Meteorology)*, 0889, <http://dx.doi.org/10.3402/tellusb.v51i1.16264>.
- d-maps-1 (2020a). *Map of Europe*. d-maps.com, https://d-maps.com/carte.php?num_car=2232&lang=en. (Accessed 24 April 2020).
- d-maps-2 (2020b). *Map of Canton Ticino*. d-maps.com, https://d-maps.com/carte.php?num_car=10350&lang=en. (Accessed 24 April 2020).
- Dale, D. J. (2006). Statistical comparisons of classifiers over multiple data sets. *Journal of Machine Learning Research*, 7(1), 1–30.

- Duan, T., Avati, A., Ding, D. Y., Thai, K. K., Basu, S., Ng, A. Y., et al. (2019). NGBoost: Natural Gradient Boosting for Probabilistic Prediction. <http://arxiv.org/abs/1910.03225>.
- Eslami, E., Choi, Y., Lops, Y., & Sayeed, A. (2019). A real-time hourly ozone prediction system using deep convolutional neural network. *Neural Computing and Applications*, 0123456789, 8–11. <http://dx.doi.org/10.1007/s00521-019-04282-x>, <https://doi.org/10.1007/s00521-019-04282-x>.
- Feng, Y., Zhang, W., Sun, D., & Zhang, L. (2011). Ozone concentration forecast method based on genetic algorithm optimized back propagation neural networks and support vector machine data classification. *Atmospheric Environment*, 45(11), 1979–1985. <http://dx.doi.org/10.1016/j.atmosenv.2011.01.022>, <http://dx.doi.org/10.1016/j.atmosenv.2011.01.022>.
- Gneiting, T., & Raftery, A. E. (2007). Strictly proper scoring rules, prediction, and estimation. *Journal of the American Statistical Association*, 102(477), 359–378. <http://dx.doi.org/10.1198/016214506000001437>.
- Gong, B., & Ordieres-Meré, J. (2016). Prediction of daily maximum ozone threshold exceedances by preprocessing and ensemble artificial intelligence techniques. *Environmental Modelling & Software*, 84(C), 290–303. <http://dx.doi.org/10.1016/j.envsoft.2016.06.020>, <https://doi.org/10.1016/j.envsoft.2016.06.020>.
- Hastie, T., Tibshirani, R., & Friedman, J. (2009). The elements of statistical learning. *Elements*, 1, 337–387. <http://dx.doi.org/10.1007/b94608>, URL: <http://www.springerlink.com/index/10.1007/b94608>.
- Hollander, M., & Wolfe, D. (1999). *A volume in the wiley series in probability and mathematical statistics, Nonparametric statistical methods* (2nd ed.).
- Kourentzes, N., Svetunkov, I., & Schaer, O. (2020). <https://github.com/trnnick/tsutils/>.
- Kupilik, M., & Witmer, F. (2018). Spatio-temporal violent event prediction using Gaussian process regression. *Journal of Computational Social Science*, 1(2), 437–451. <http://dx.doi.org/10.1007/s42001-018-0024-y>, <https://doi.org/10.1007/s42001-018-0024-y>.
- Lu, X., Zhang, L., & Shen, L. (2019). Meteorology and climate influences on tropospheric ozone: a review of natural sources, chemistry, and transport patterns. *Current Pollution Reports*, 5(4), 238–260. <http://dx.doi.org/10.1007/s40726-019-00118-3>.
- Lundberg, S. M., Erion, G., Chen, H., DeGrave, A., Prutkin, J. M., Nair, B., et al. (2020). From local explanations to global understanding with explainable ai for trees. *Nature Machine Intelligence*, <http://dx.doi.org/10.1038/s42256-019-0138-9>.
- Lundberg, S. M., & Lee, S. I. (2017). A unified approach to interpreting model predictions. *Advances in Neural Information Processing Systems*.
- Lv, B., Cobourn, W. G., & Bai, Y. (2016). Development of nonlinear empirical models to forecast daily PM_{2.5} and ozone levels in three large Chinese cities. *Atmospheric Environment*, 147, 209–223. <http://dx.doi.org/10.1016/j.atmosenv.2016.10.003>, <http://dx.doi.org/10.1016/j.atmosenv.2016.10.003>.
- Meinshausen, N. (2014). Quantile regression forests. *Journal of Machine Learning Research*, 131, 65–78. <http://dx.doi.org/10.1016/j.jmva.2014.06.005>.
- Mohan, S., & Saranya, P. (2019). A novel bagging ensemble approach for predicting summertime ground-level ozone concentration. *Journal of the Air and Waste Management Association*, 69(2), 220–233. <http://dx.doi.org/10.1080/10962247.2018.1534701>, <https://doi.org/10.1080/10962247.2018.1534701>.
- Monks, P. S., Archibald, A. T., Colette, A., Cooper, O., Coyle, M., Derwent, R., et al. (2015). Tropospheric ozone and its precursors from the urban to the global scale from air quality to short-lived climate forcer. *Atmospheric Chemistry and Physics*, 15(15), 8889–8973. <http://dx.doi.org/10.5194/acp-15-8889-2015>.
- Pinson, P., McSharry, P., & Madsen, H. (2010). Reliability diagrams for non-parametric density forecasts of continuous variables: Accounting for serial correlation. *Quarterly Journal of the Royal Meteorological Society*, 136(646), 77–90. <http://dx.doi.org/10.1002/qj.559>.
- Pusede, S. E., Gentner, D. R., Wooldridge, P. J., Browne, E. C., Rollins, A. W., Min, K. E., et al. (2014). On the temperature dependence of organic reactivity, nitrogen oxides, ozone production, and the impact of emission controls in San Joaquin Valley, California. *Atmospheric Chemistry and Physics*, 14(7), 3373–3395. <http://dx.doi.org/10.5194/acp-14-3373-2014>.
- Pusede, S. E., Steiner, A. L., & Cohen, R. C. (2015). Temperature and recent trends in the chemistry of continental surface ozone. *Chemical Reviews*, 115(10), 3898–3918. <http://dx.doi.org/10.1021/cr5006815>.
- Sheta, A., Faris, H., Rodan, A., Kovač-Andrić, E., & Al-Zoubi, A. M. (2018). Cycle reservoir with regular jumps for forecasting ozone concentrations: Two real cases from the east of Croatia: CRJ for forecasting ozone concentrations. *Air Quality, Atmosphere and Health*, 11(5), 559–569. <http://dx.doi.org/10.1007/s11869-018-0561-9>.
- Siwek, K., & Osowski, S. (2016). Data mining methods for prediction of air pollution. *International Journal of Applied Mathematics and Computer Science*, 26(2), 467–478. <http://dx.doi.org/10.1515/amcs-2016-0033>.
- Stewart, D. R., Saunders, E., Perea, R. A., Fitzgerald, R., Campbell, D. E., & Stockwell, W. R. (2017). Linking air quality and human health effects models: An application to the Los Angeles air basin. *Environmental Health Insights*, 11, <http://dx.doi.org/10.1177/1178630217737551>.
- Swiss Society of Air Protection Officers (2019). Indice de pollution de l'air à court terme IPC. (in French). URL: https://cerclair.ch/assets/pdf/27a_2019_08_28_F_Indice_de_pollution_de_lair_court_terme.pdf.
- The Swiss Federal Council (1985). Ordinance on Air Pollution Control (OAPC). URL: <https://www.admin.ch/opc/en/classified-compilation/19850321/index.html>.
- Tibshirani, R. (1996). Regression shrinkage and selection via the Lasso. *Journal of the Royal Statistical Society. Series B. Statistical Methodology*, 58(1), 267–288.
- Walcek, C. J., & Yuan, H. H. (1995). Calculated influence of temperature-related factors on ozone formation rates in the lower troposphere. *Journal of Applied Meteorology*, [http://dx.doi.org/10.1175/1520-0450\(1995\)034<1056:CIOTRF>2.0.CO;2](http://dx.doi.org/10.1175/1520-0450(1995)034<1056:CIOTRF>2.0.CO;2).
- World Health Organization (2003). *Health aspects of air pollution with particulate matter, ozone and nitrogen dioxide. Report on a WHO working group* (p. 95). Bonn, Germany: Regional Office for Europe, http://www.euro.who.int/_data/assets/pdf_file/0005/112199/E79097.pdf.